Oxid Met (2018) 89:713–730
https://doi.org/10.1007/s11085-017-9817-2

ORIGINAL PAPER

The Influence of Temperature on the Oxidation Mechanism in Air of HR3C and Aluminum-Containing 22Cr–25Ni Austenitic Stainless Steels

Jian Wang[1] · Yongfeng Qiao[1] · Nan Dong[1] · Xudong Fang[2] · Xin Quan[1] · Yishi Cui[1] · Peide Han[1]

Received: 27 April 2017 / Revised: 25 October 2017 / Published online: 25 January 2018

Abstract To evaluate the suitability of HR3C and 22Cr–25Ni–2.5Al AFA steels as the heat-resistant alloys, the oxidation behavior of them was investigated in air at 700, 800, 900 and 1000 °C. The evolution of oxide layer on the surface and subsurface was investigated using a combination of compositional/elemental (SEM, EDS) and structural (XRD, GDOES) techniques. A dense and continuous Cr_2O_3 healing layer on the HR3C was formed at the temperature of 700 or 800 °C, but the Cr_2O_3 oxide film on HR3C was unstable and partly converted into a less protective $MnCr_2O_4$ with the increase in temperature to 900 or 1000 °C. The composition and structure of oxide film of 22Cr–25Ni–2.5Al AFA steels are significantly different to the HR3C alloys. The outer layer oxides transformed from Cr_2O_3 to Al-containing oxides, leading to a better oxidation resistance at 700 or 800 °C compared to HR3C. Further, the oxide films consist of internal Al_2O_3 and AlN underneath the outer loose layer after 22Cr–25Ni–2.5Al AFA oxidized at 900 or 1000 °C. It can be proved that the internal oxidation and nitrogen would make 22Cr–25Ni–2.5Al AFA steels have worse oxidation resistance than HR3C alloys at 900 or 1000 °C.

Keywords HR3C · Alumina-forming austenitic steel · Internal oxidation · Nitridation · High-temperature oxidation

✉ Jian Wang
jianwang1@126.com

✉ Peide Han
hanpeide@126.com

[1] College of Materials Science and Engineering, Taiyuan University of Technology, Taiyuan 030024, Shanxi, China

[2] Technology Center of Shanxi Taigang Stainless Steel Co. Ltd., Taiyuan 030003, Shanxi, China

Introduction

Heat-resistant steels are widely applied in diesel engines, turbine engines and other steam boiler units at high temperatures and/or in harsh environments [1, 2]. Some new steels, including low-alloy steels, ferritic stainless steels (such as T/P23 and T/P24) and austenitic stainless steels (such as Super 304H, TP347HFG and HR3C), have been synthesized to meet the material requirement in these fields [3]. HR3C steel, which has excellent high-temperature corrosion resistance and superior creep strength, has been the preferred material for heat exchangers and reactor pressure vessels. Currently, many studies have focused on the high-temperature creep resistance and corrosion resistance of HR3C heat-resistant steels [4–9]. Few works have highlighted that the changes in oxidization resistance performances are influenced by temperature and grain size [4]. Some studies discussed the high-temperature corrosion behavior of HR3C austenitic steel in Na_2SO_4–K_2SO_4 molten salt [5]. Several studies emphasized the change in precipitate phase during the high-temperature creep process [6, 7]. In other words, the Cr elements of HR3C diffuse from the matrix to the surface, which results in the formation of Cr_2O_3, protecting the steel from the hostile environment. However, the Cr_2O_3 films on heat-resistant steels are not stable when the oxidation temperature is greater than 650 °C and accompanied by the formation of $CrO_2(OH)_2$ at steam temperature [10].

Because the $A1_2O_3$ has a better stability than Cr_2O_3, Al has been added as an active element to improve the oxidation resistance of steels [11–13]. The creep-resistant, Al_2O_3-forming austenitic (AFA) stainless steels were first developed in 2007, with strengthening achieved through nanodispersions of NbC in the matrix [14]. Subsequently, the AFA steels have drawn much attention. Brady et al. [15, 16] prepared a series of AFA steels based on Fe–15Cr–20Ni alloy compositions by adding Al with different contents and studied the role of alloying elements in the anti-creep and anti-oxidation aspects at high temperature. Lu et al. [17, 18] also smelted AFA steels based on Fe–18Cr–25Ni alloy compositions. The corresponding precipitation strength mechanism and high-temperature oxidation resistance performance were discussed. Recently, AFA steels with different Al contents (1.5, 2.5 and 3.5 wt%) were also prepared by our laboratory based on the composition of the 22Cr–25Ni steel, which shows a better oxidation resistance than HR3C austenitic steels [19, 20].

The Cr_2O_3 or Al_2O_3 oxide films formed on the surface of heat-resistant steels often play an important role in protecting the alloy from high-temperature corrosion. With the increase in service temperature or service time, the cracking or spalling of the oxide film from the surface is also inevitable. Numerous investigations related to heat-resistant alloys reported the formation and breakdown of the oxide films on the matrix. The microstructure evolution of chromium-containing austenitic heat-resistant steels after breakaway oxidation was examined, and a two-layer oxide scale was observed to form on the surface, composed of a dense and adherent inner sublayer of Cr_2O_3 and an outer sublayer of spinel-type oxide $MnCr_2O_4$ [21–24]. For AFA steels, it was found that the alloys have an excellent oxidation resistance of up to 800–1100 °C depending on the composition and exposure conditions [25–27];

however, they are susceptible to attacks of AlN particles formed at higher temperatures [28, 29]. Nevertheless, there are few studies and comparisons on the oxidation resistance mechanism of oxide films on HR3C and alumina-containing 22Cr–25Ni austenitic stainless steels after high-temperature oxidation at different temperatures.

In this study, the high-temperature oxidation kinetic processes of HR3C and 22Cr–25Ni–2.5Al AFA alloys at 700, 800, 900 and 1000 °C are investigated. Furthermore, the microstructure and composition of oxidation films on the heat-resistant steels were further analyzed by scanning electron microscope (SEM), energy-dispersive spectrometer (EDS), X-ray diffraction (XRD) and glow discharge optical emission spectroscopy (GDOES). The oxidation resistance mechanism of HR3C and 22Cr–25Ni–2.5Al AFA alloy was examined by comparing the change law of oxidation films at different temperatures. This research intends to provide an intensive understanding of alloy design strategy on heat-resistant steels.

Experimental Procedures

Material Preparation

Ingots of each given composition were prepared in a 50-kg vacuum induction furnace using commercially pure elements. After melting and casting, the ingots were hot-rolled into slabs with a thickness of 20 mm. Then, the alloys were solution-heat-treated at 1250 °C for 2 h and subsequently water-quenched to prevent precipitation of the second phase. Analyzed compositions of HR3C and AFA steels that were confirmed by an ICP spectrometer are shown in Table 1.

High-Temperature Oxidation Testing

The material was cut using the electrical discharge machining technique to yield square test coupons with dimensions of 15 mm × 13 mm × 3.5 mm. Prior to the oxidation tests, all the specimens were carefully ground with SiC paper on all sides up to 1200 grit and then cleaned in ethanol by an ultrasonic bath to degrease the surfaces. Isothermal oxidation tests were carried out at 700, 800, 900 and 1000 °C in laboratory air for different times, respectively. The specimens were put in individual alumina crucibles to collect the spalled oxide. After exposure to the designated temperature for a given duration, the alumina crucibles together with the specimens were removed from the furnace and cooled in air with an estimated

Table 1 Composition of HR3C and AFA steels with a 22Cr–25Ni–2.5Al composition

Alloy	Cr	Ni	Al	Nb	Mn	Cu	Si	C	N	Fe
22Cr–25Ni–2.5Al	21.36	24.59	2.48	0.42	0.77	2.65	0.18	0.06	–	Bal.
HR3C	24.64	19.42	–	0.37	1.44	0.04	0.38	0.06	0.28	Bal.

cooling time of approximately 30 min to room temperature. The weight of each tested sample before and after exposure was measured using an electronic balance with an accuracy of 0.1 mg, and the oxidation kinetics of experimental steel was drawn in accordance with weight gain over time. Afterward, the oxidized samples were embedded in Bakelite (in order to protect the oxide scale formed), ground with SiC abrasive papers from no. 100 to 2000, and then mechanically polished using 1- and 0.3-μm alumina suspension.

Characterization

The morphologies of the surface and cross section of the specimens after oxidation were further analyzed using a TESCAN MIRA3 SEM equipped with an EDS. The constituent phases of oxidation products were determined using DX-2700 XRD apparatus with Cu target. GDOES was used to identify the depth distribution of elements in the oxide scale. Samples for transmission electron microscope (TEM) observation were prepared by an ion slicer (JEOL EM-09100IS, Tokyo, Japan) on the cross section perpendicular to the oxide growth direction. The detailed interface structure was observed on a TEM (Topcon EM-002B, Topcon Corporation, Tokyo, Japan) operated at 200 kV.

Results

Oxidation Kinetic Analysis

Figure 1 shows the isothermal oxidation kinetic curves of HR3C and 22Cr–25Ni–2.5Al austenitic stainless steels oxidized in air at 700, 800, 900 and 1000 °C. As shown in Fig. 1a, the oxidation rate in HR3C was rapid in the initial stage. However, when the oxide layer was formed on the surface of HR3C, the oxidation rate gradually slowed down. Moreover, the weight gain after the oxidation in 900 and 1000 °C was significantly higher than that in 700 and 800 °C, implying the

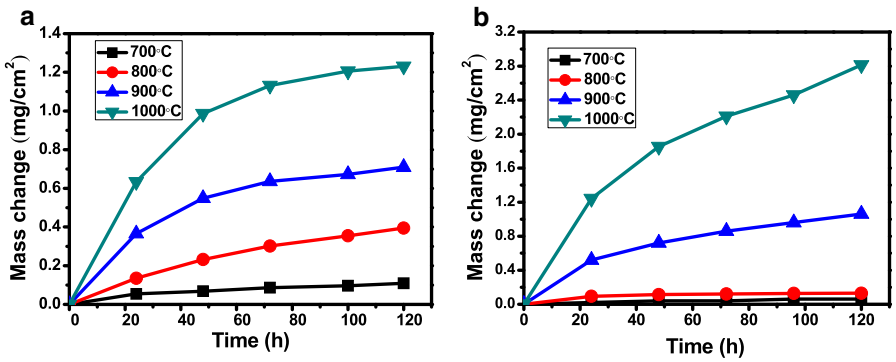

Fig. 1 Isothermal oxidation kinetics of HR3C stainless steels (**a**) and 22Cr–25Ni–2.5Al AFA steels (**b**) after oxidation at different temperatures for various oxidation durations

strong effect of temperature on the oxidation process of HR3C. For the 22Cr–25Ni–2.5Al AFA steel, it can be observed from Fig. 1b that the weight gain of this steel is extremely small at 700 and 800 °C exposure temperatures, suggesting the low oxidation rate at this temperature. However, the weight gain increased significantly when the sample was oxidized at 900 and 1000 °C, which suggests that the oxide film on the surface cannot provide an effective protection.

The oxidation kinetics was further simulated by using the following model:

$$\Delta w = k_{\mathrm{p}} t^{1/m}, \tag{1}$$

where Δw is the weight gain per unit area, t is the exposure time, k_{p} is a proportionality coefficient, and m is the rate exponent [6]. The oxidation rate is presented in Table 2. It is observed that most of the alloys approximately exhibited a square parabolic law. The parabolic rate constant, k_{p}, at each temperature was also calculated, and the results are tabulated in Table 2. Figure 2 shown tha kinetics of isothermal oxidation of HR3C and 22Cr-25Ni-2.5Al alloy followed the power-law fitting results. The kinetic rates of normal HR3C oxidized at 700 °C [9] and AFA steels with a composition about 18Cr–25Ni–3Al oxidized at 800 °C [17] obtained from the literature were further fitted and were about 1.11×10^{-4} and 0.33×10^{-4} mg/cm^2, similar to the results in our experiment from the order of magnitude. The effect of temperature on the oxidation behavior of the two alloys can be expressed by the Arrhenius equation,

$$k_{\mathrm{p}} = k_0 \exp\left(-\frac{Q}{RT}\right) \tag{2}$$

where k_0 is a constant, Q is the activation energy, T is the absolute temperature, and R is the universal gas constant. By plotting k_{p} versus the reciprocal of temperature, the activation energy of the oxidation can be derived from the slopes of the fitting lines, as shown in Fig. 3. For the HR3C and 22Cr–25Ni–2.5Al alloys, the activation energies were calculated to be about 168.94 and 279.11 kJ/mol, respectively, suggesting that Al has a positive effect on the oxidation resistance.

Table 2 Oxidation rate equations for HR3C and 22Cr–25Ni–2.5Al AFA steels

Alloy	Temperature (°C)	Fitting equation	Fitting similarity (R)	The parabolic rate constant (k_{p}, mg/cm^2)
HR3C	700	$\Delta m = 0.0126t^{1/2.2272}$	0.9891	9.545×10^{-5}
	800	$\Delta m = 0.0200t^{1/1.5944}$	0.9894	0.00134
	900	$\Delta m = 0.1220t^{1/2.6688}$	0.9558	0.00419
	1000	$\Delta m = 0.1879t^{1/2.4913}$	0.9534	0.01411
Fe–22Cr–25Ni–2.5Al	700	$\Delta m = 0.0054t^{1/2.1277}$	0.9833	3.331×10^{-5}
	800	$\Delta m = 0.0524t^{1/2.1894}$	0.9662	1.277×10^{-4}
	900	$\Delta m = 0.1327t^{1/2.3001}$	0.9984	0.00387
	1000	$\Delta m = 0.2764t^{1/2.0683}$	0.9920	0.03897

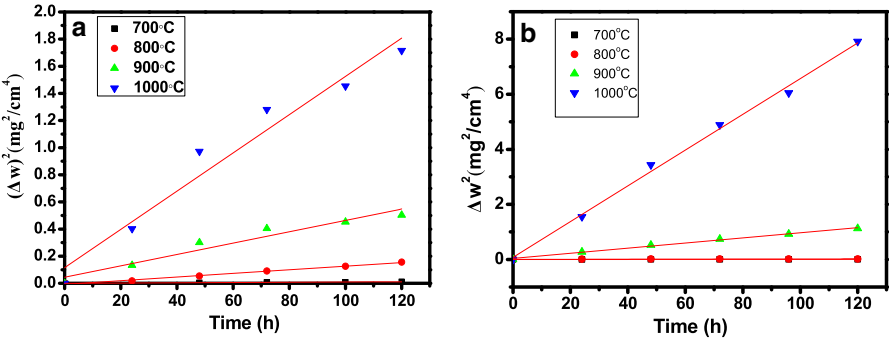

Fig. 2 Kinetics of isothermal oxidation of HR3C (**a**) and 22Cr–25Ni–2.5Al alloy (**b**) followed the power-law fitting results

Surface Morphology After Oxidation

The surface morphology of the oxide film on HR3C oxidized at different temperatures was characterized by the SEM measurement and is shown in Fig. 4a, c, e, g, corresponding to the specimens oxidized at 700, 800, 900 and 1000 °C, respectively. Figure 4b, d, f, h shows the enlarged images for certain positions in Fig. 4a, c, e, g, respectively. It can be observed that the surface of HR3C oxidized at 700 °C was fully coated by oxides with small sizes, but the oxides on the surface of HR3C were rod shaped when the oxidation temperature was increased to 800 °C. The oxides further grew during the oxidation at 900 °C. By increasing further the oxidation temperature to 1000 °C, the morphology of oxides has a huge change and some concave holes were also observed. The chemical composition of the oxide films at 1, 2, 3 and 4 was analyzed according to the EDS point analysis results and is given in Table 3. According to the analysis, the oxide film on HR3C formed at a relatively low temperature (700 or 800 °C) mainly consists of O and Cr elements, but the ratio of Fe and Mn elements is significantly higher on the oxide films of HR3C oxidized at a relatively high temperature (900 or 1000 °C).

The surface morphology of the oxide film on the 22Cr–25Ni–2.5Al AFA steel was also characterized by SEM as shown in Fig. 5a, c, e, g, corresponding to the

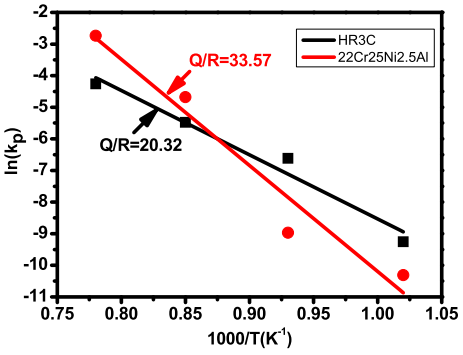

Fig. 3 Arrhenius plot for the oxidation of HR3C and 22Cr–25Ni–2.5Al alloys

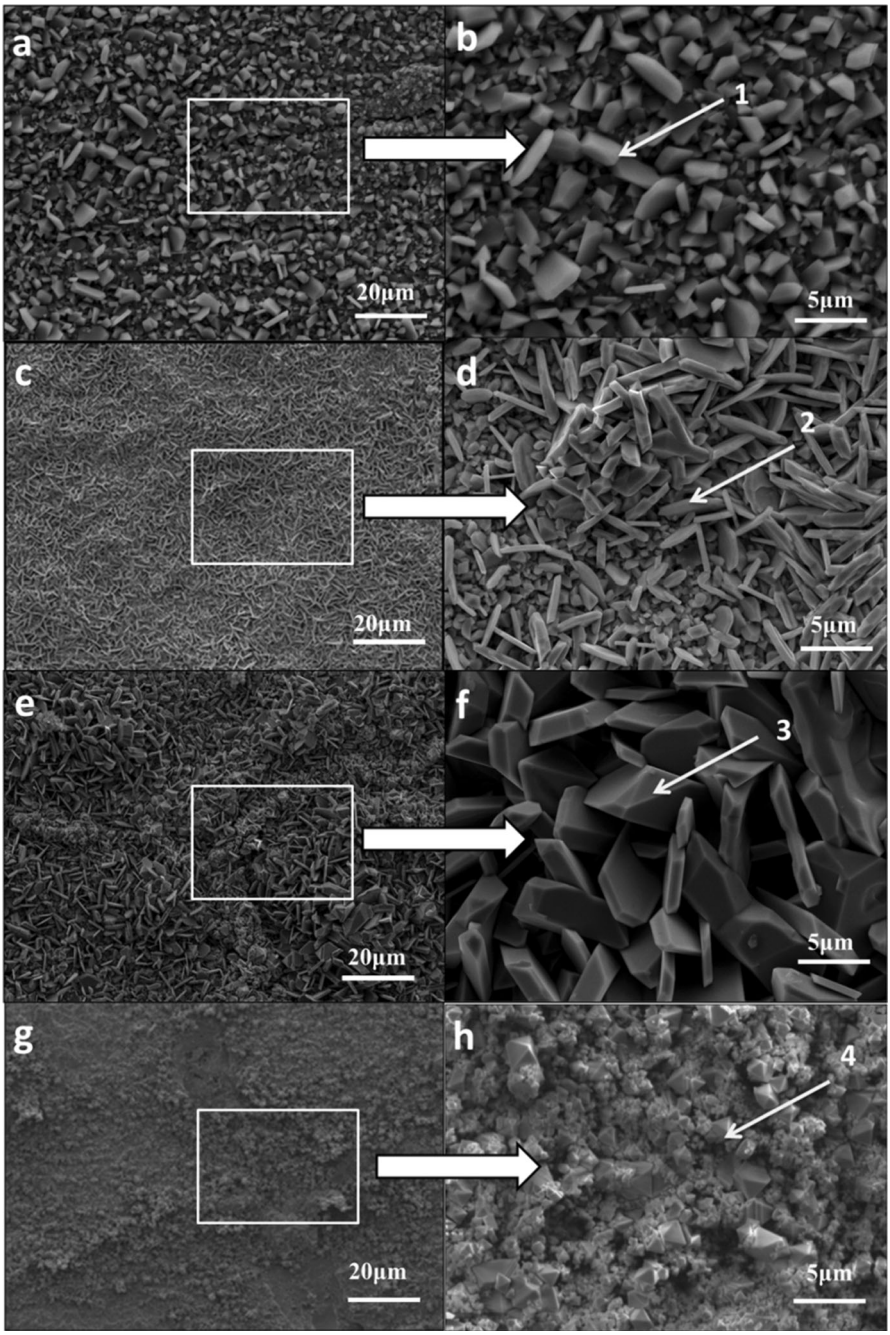

Fig. 4 Surface SEM images for the HR3C oxidized at different temperatures: **a** 700, **b** 800, **c** 900 and **d** 1000 °C

Table 3 EDS point analysis results (at.%) at 1, 2, 3 and 4 for alloy samples shown in Fig. 4 (after oxidation at different temperatures for 120 h)

Area	O	Cr	Fe	Mn	Ni
1	54.2	40.9	2.0	2.9	0.0
2	58.9	46.9	2.3	4.2	0.0
3	42.7	45.4	6.3	4.9	0.9
4	52.1	28.5	2.7	16.7	0.0

specimens oxidized at 700, 800, 900 and 1000 °C, respectively. Figure 5b, d, f, h shows the enlarged images for certain positions in Fig. 5a, c, e, g, respectively. The oxide films oxidized at 700 °C are very thin and smooth, and some granulated oxides were distributed on the surface. However, when the temperature was increased to the 800 °C, some regions were coated by oxides on a larger scale, besides the granulated oxides. Furthermore, the entire surface was covered by oxides with a large size and the oxide films become thicker at the 900 °C oxidizing temperature. After the oxidized temperature was increased to 1000 °C, it can be observed that some oxides were spalled and the oxide morphology has a significant change. The EDS point analysis results (at.%) at 1, 2, 3 and 4 for alloy samples shown in Fig. 5 (after oxidation at different temperatures for 120 h) are presented in Table 4. From the above results, it can be inferred that there was an evident agglomeration of Al and O at the relatively low oxidation temperatures of 700 or 800 °C, indicating the formation of Al_2O_3 on the surface of 22Cr–25Ni–2.5Al AFA steels. However, after oxidation at 900 and 1000 °C, the ratio of Fe and Mn elements increased and the ratio of Al elements decreased on the oxide films of the AFA elements.

Examination of Cross Sections

The cross section morphologies of the HR3C steel specimens oxidized at 700, 800, 900 and 1000 °C for 120 h are shown in Fig. 6. It is evident that a chromium-containing oxide layer identified by the compositional profile was formed on the surface of HR3C, when it was oxidized at 700 and 800 °C. According to the experiments done by Evans et al. [30], at least 16 wt% Cr in alloys is required to guarantee a healing layer in the temperature range from 750 to 900 °C for Fe–20Cr–25Ni steel. Thus, the 25 wt% Cr in HR3C is sufficient to sustain the formation of Cr_2O_3 at temperature of 700 or 800 °C, which is similar to that observed in the surface morphology shown in Fig. 4a, b. It has been reported that the oxide scale would become duplex with spinel formation on the top surface and Cr_2O_3-type oxide as inner scale, after the oxidation of austenitic stainless steels was broken down [23]. As the temperature increases to 900 and 1000 °C, it can also be observed that the Cr_2O_3 oxide layer was destroyed and gradually became uncompact, owing to the diffusion of Fe and Mn into the Cr_2O_3 oxide films. The observable Fe-rich and Mn-rich parts were distributed on the top of oxide layer, with the HR3C oxidation at 1000 °C. Meanwhile, some internal Cr_2O_3 particles that were confirmed by the EDS

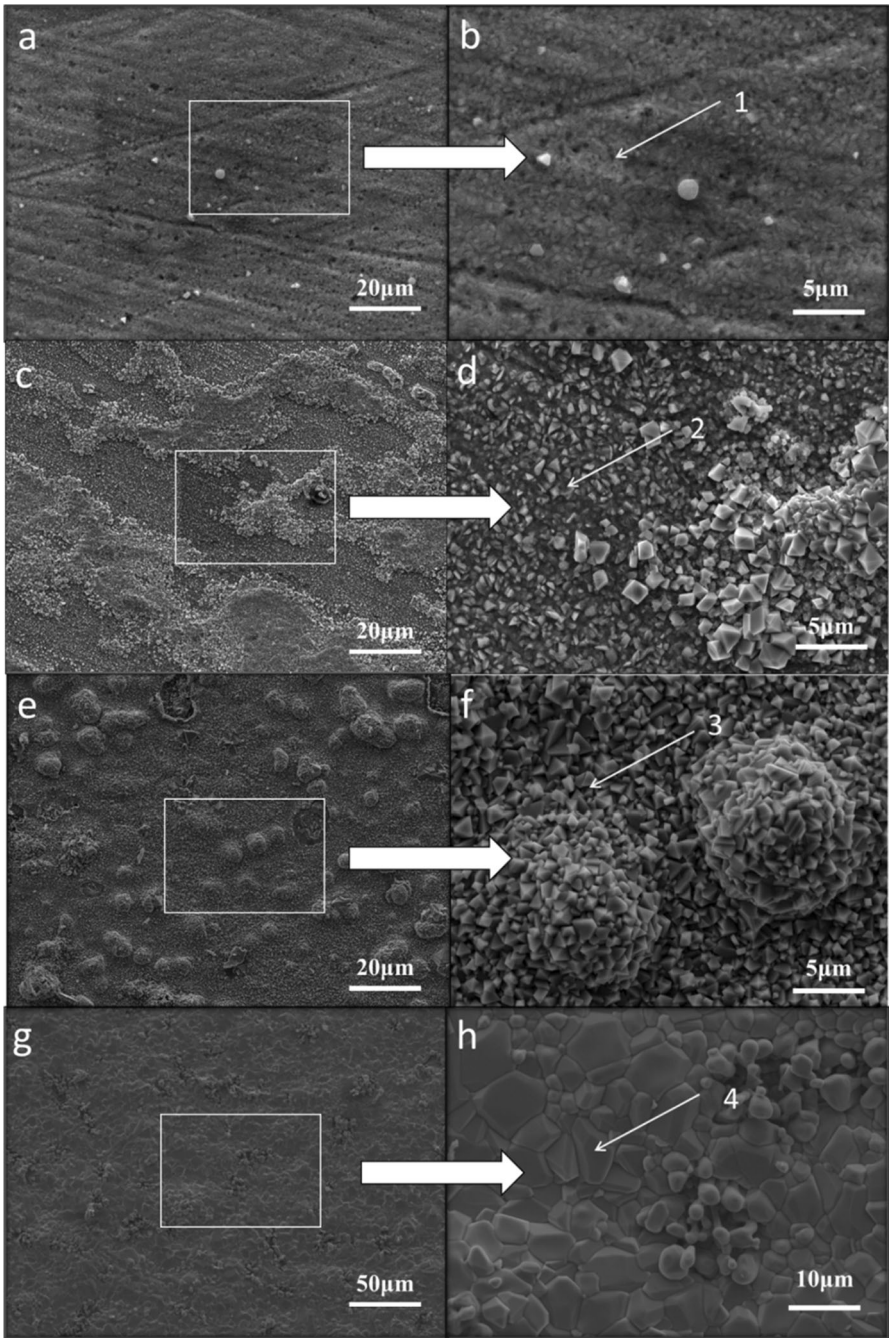

Fig. 5 Surface SEM images for the 22Cr–25Ni–2.5Al AFA steels oxidized at different temperatures: **a** 700, **b** 800, **c** 900 and **d** 1000 °C

(not shown in the results) also exist below the outer layer oxides. To further confirm the element distribution on the oxide layer, line profiles on cross section of oxide scale for HR3C oxidized at 800 and 1000 °C were measured. As shown in Fig. 7, it can be seen that only Cr and O exist on the oxide scale at 800 °C, but the Mn was also found on the oxide scale at 1000 °C besides the Cr and O, suggesting the diffusion of Mn from matrix into surface with the increase in temperature. A cross-sectional TEM image of the oxide scale of the HR3C alloy after oxidation at 1000 °C for 120 h is also shown in Fig. 8. Figure 8a shows the bright-field image of the metal scale and scale–gas interfaces. The selected area diffraction (SAD) pattern shown in Fig. 8b demonstrates that the grains circled by red line correspond to Cr_2O_3, and EDS shown in Fig. 8c further confirms it. Besides that, some Mn-rich elements shown in Fig. 8d were also found in the grains, meaning the formation of $MnCr_2O_4$, which may be explained by further reaction at high temperature between Cr_2O_3 and the diffused Mn element.

Figure 9 further shows the cross section morphologies of 22Cr–25Ni–2.5Al AFA alloys exposed in air at different temperatures for 120 h. When the oxide temperature is 800 °C, the elemental mapping of scale suggests that the oxide film is mainly compact and continuous alumina, which appears to have a good adherence to the matrix, and there are no adverse precipitates under the oxide films. The reason for the formation of Al_2O_3 is discussed in our previous work [19]. However, a mixture of Cr-containing and Mn-containing oxide layer retained on the top and internal oxidation and nitration are observed in the sample exposed to air only at 900 or 1000 °C. A more careful investigation indicates that the needle-like particles that principally contained Al and N started to grow downward to the oxide layer. Moreover, AlN precipitates tend to gradually increase with rising oxidation temperatures. Figure 10 further shows the cross section morphologies of 22Cr–25Ni–2.5Al AFA steel oxidized at 1000 °C for 24, 72 and 120 h. The thickness of the outer $MnCr_2O_4$ layer is increasing with oxidation time, and the AlN is also becoming deeper with exposure times. A cross-sectional TEM image of the oxide scale of the 22Cr–25Ni–2.5Al alloy after oxidation at 1000 °C for 120 h is shown in Fig. 11. Figure 11a shows the bright-field image of the metal scale and scale–gas interfaces. Similar to the HR3C, the composition of oxide film mainly consists of Cr_2O_3 and $MnCr_2O_4$; besides that, some Cr_2O_3 and Al_2O_3 grains was also found underneath the oxide scale, which can be proved by the SAED and EDS analysis.

Table 4 EDS point analysis results (at.%) at 1, 2, 3 and 4 for alloy samples shown in Fig. 3 (after oxidation at different temperatures for 120 h)

Area	O	Cr	Fe	Mn	Ni	Al
1	44.2	11.3	13.7	1.8	4.4	24.6
2	59.6	3.4	0.8	0.6	0.5	35.1
3	58.2	20.2	4.6	16.1	0.9	0.0
4	61.5	11.1	6.3	18.1	2.7	0.3

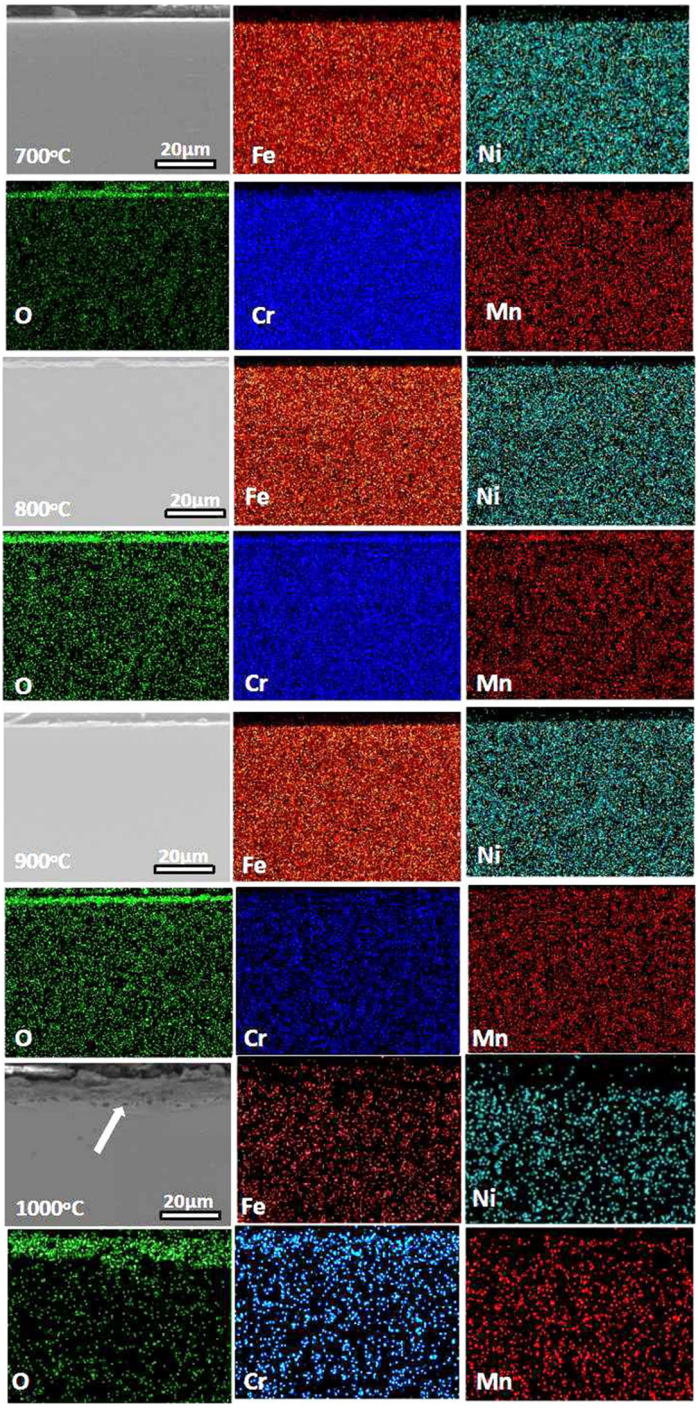

Fig. 6 Compositional mapping of oxide layer in HR3C alloys, exposed in air at different temperatures for 120 h

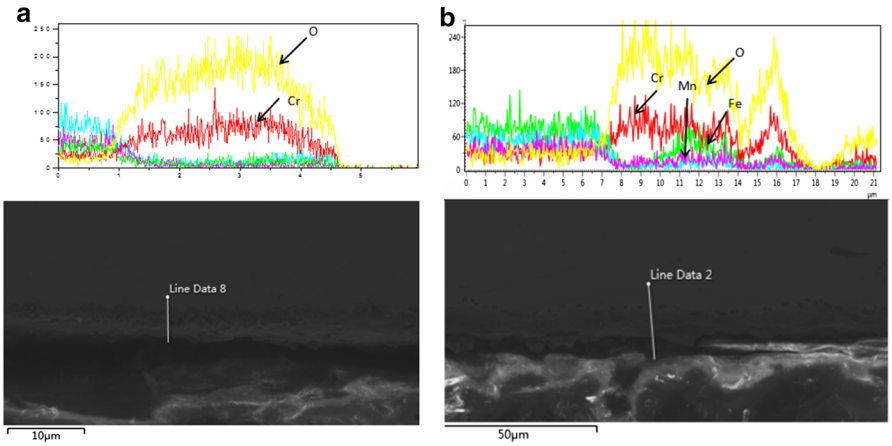

Fig. 7 Line profiles on cross section of oxide scale for HR3C oxidized at 800 and 1000 °C

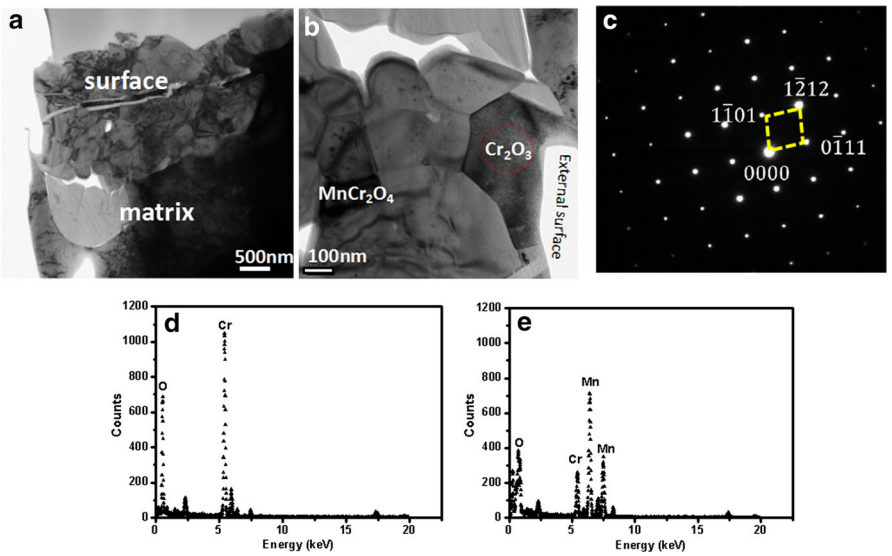

Fig. 8 TEM observation of oxide scale of HR3C alloy after oxidation in air at 1000 °C for 120 h: **a** bright-field image of the metal scale and scale–gas interfaces; **b** bright-field image of grains; **c** SAED pattern of Cr_2O_3; **d** EDS of Cr_2O_3; **e** EDS of $MnCr_2O_4$

Phase Characterization of Oxide Scale

Figure 12 shows the XRD of the oxidation film on HR3C and 22Cr–25Ni–2.5Al AFA steels that were oxidized at 800 and 1000 °C. Owing to the thin oxide films formed on the heat-resistant steels, the diffraction peaks of the austenite matrix appeared with high intensity in all the samples oxidized at different temperatures. However, the structures of the oxide film on the steels oxidized at 800 and 1000 °C

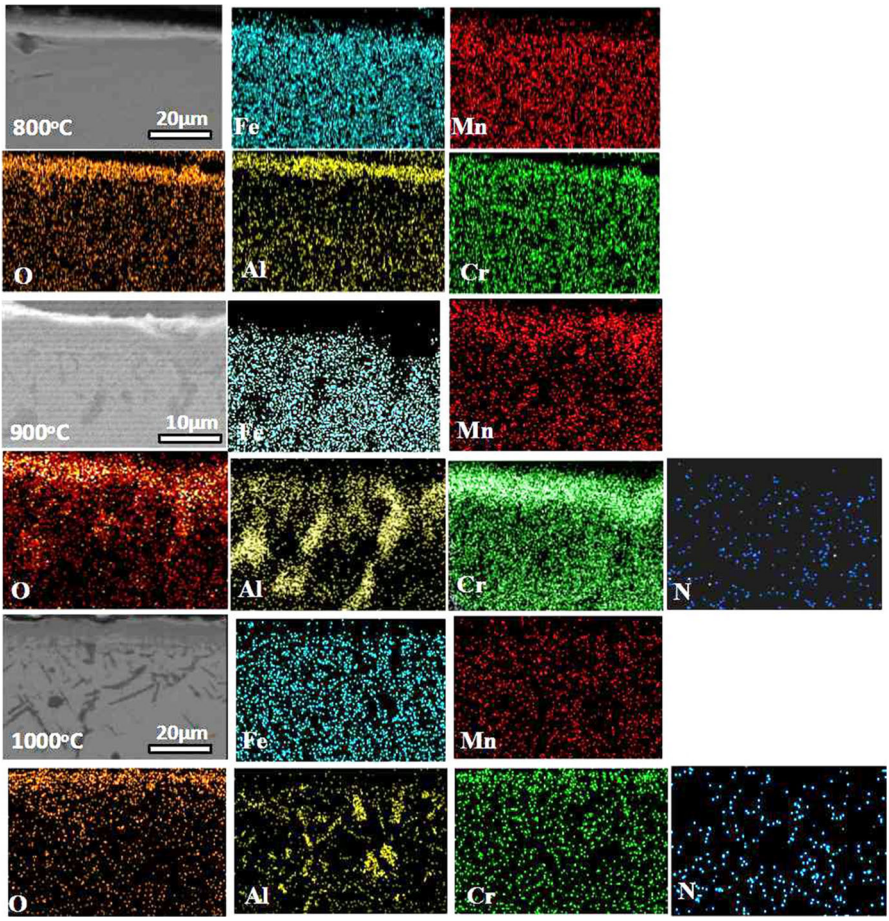

Fig. 9 Compositional mapping of oxide layer in Fe–22Cr–25Ni–2.5Al AFA alloys, exposed in air at different temperatures for 120 h

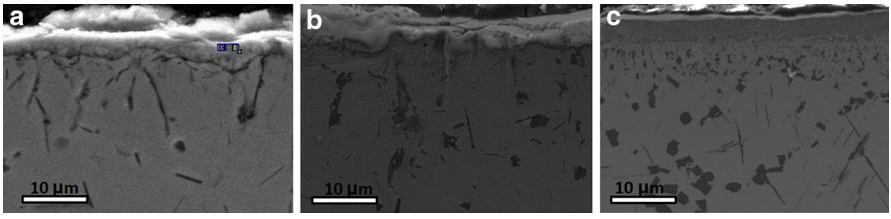

Fig. 10 Cross section morphology of 22Cr–25Ni–2.5Al AFA steels oxidized at 1000 °C for different times: **a** 24 h, **b** 72 h and **c** 120 h

are very different. For HR3C, after oxidation at 800 °C, the strongest peak intensity of Cr_2O_3 among the phases was observed; hence, it can be concluded that Cr_2O_3 is the main oxide when HR3C was oxidized in 800 °C. However, the XRD result of

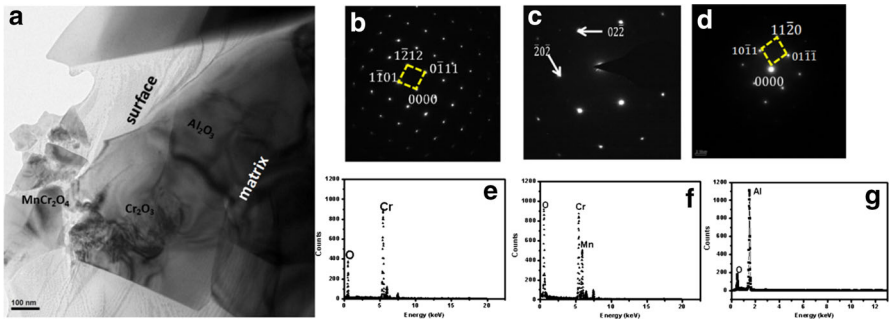

Fig. 11 TEM observation of oxide scale of 22Cr–25Ni–2.5Al alloy after oxidation in air at 1000 °C for 120 h: **a** bright-field image of the metal scale and scale–gas interfaces; **b** SAED pattern of Cr_2O_3; **c** SAED pattern of Cr_2O_3; **d** SAED pattern of Al_2O_3; **e** EDS of Cr_2O_3; **f** EDS of $MnCr_2O_4$; **g** EDS of Al_2O_3

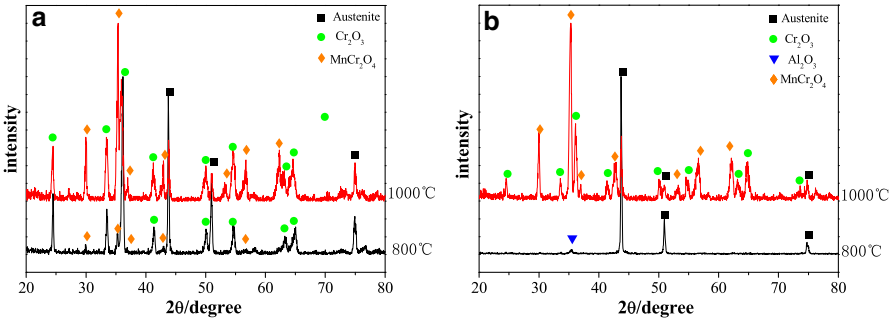

Fig. 12 XRD patterns of the oxide films formed on the HR3C (**a**) and 22Cr–25Ni–2.5Al AFA alloy (**b**)

the HR3C oxidized at 1000 °C shows that the diffraction peak intensity of Cr_2O_3 was further enhanced, and $MnCr_2O_4$ phase was also found, indicating that Mn easily diffused from the matrix into the surface through the oxidation film at this temperature, forming $MnCr_2O_4$ with Cr_2O_3 at a relatively high temperature. For 22Cr–25Ni–2.5Al, the XRD results of the sample oxidized at 800 °C indicate that the formed oxide films are mainly α-Al_2O_3, but the oxide film on the 22Cr–25Ni–2.5Al samples oxidized at 1000 °C was mainly composed of Cr_2O_3 and spinel $MnCr_2O_4$.

GDOES Analysis of the Oxide Film

In order to further confirm the changes of alloy elements in HR3C steels, GDOES was used to characterize the element dispersion on the surface and matrix of the HR3C and 22Cr–25Ni–2.5Al AFA steels oxidized at 800 and 1000 °C. As shown in Fig. 13a, it can be observed that the Cr element was rich in the surface of HR3C, which may be caused by the formation of Cr_2O_3. As the oxidation temperature increases to 1000 °C, as shown in Fig. 13c, the distribution of alloy element becomes wider than that oxidized at 800 °C, which indicates that the oxide scale

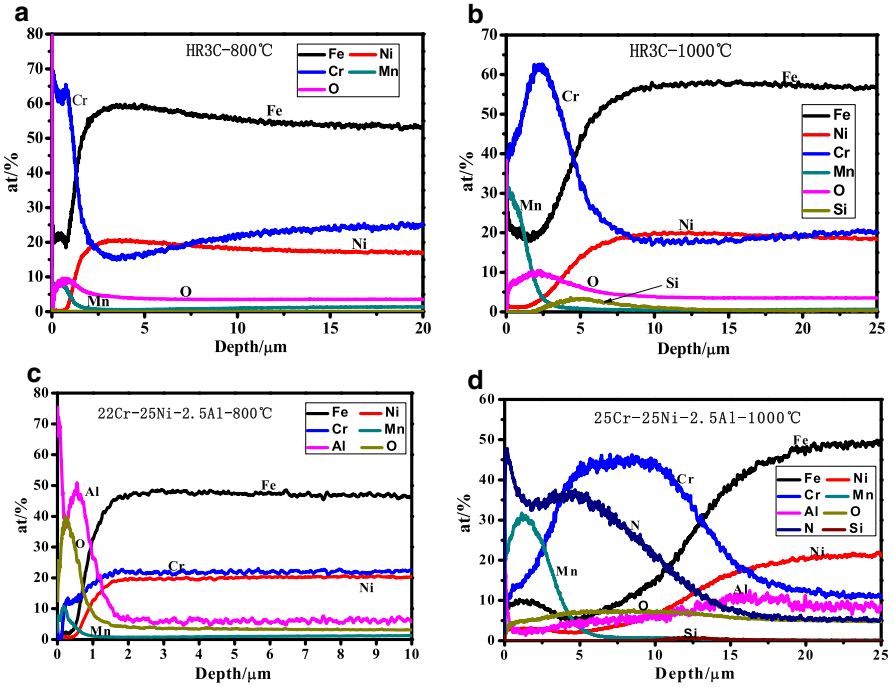

Fig. 13 GDOES of the HR3C and 22Cr–25Ni–2.5Al AFA steels oxidized at 800 (**a**, **c**) and 1000 °C (**b**, **d**)

thickness is increasing, owing to the faster diffusion rate of element and growth rate of oxide film with the increase in temperature. Moreover, the Mn content significantly increases and the Cr content decreases when the steels are oxidized at 1000 °C, suggesting that Mn rapidly moves to the outer part of the scale of Cr_2O_3 layer and the $MnCr_2O_4$ was formed by the following reaction:

$$Mn + 4/3Cr_2O_3 = 2/3Cr + MnCr_2O_4. \quad (3)$$

The 22Cr–25Ni–2.5Al AFA alloy exhibited an entirely different composition and structure of oxide films, compared to HR3C steel. As shown in Fig. 13b, the Al element up to 50 at.% is enriched in the surface and the Cr and Fe contents are extremely low at the exposure temperature of 800 °C owing to the formation of Al_2O_3 oxide films which was proved by the above-mentioned SEM and XRD results. However, it is observed from Fig. 13d that aluminum is depleted in the region closest to the surface when the oxidation is at 1000 °C. Instead, Mn is rich in the surface and exhibits a higher content than that in the samples oxidized at 800 °C. In addition, nitrogen is enriched deeper into the structure in the 22Cr–25Ni–2.5Al AFA alloy, which was caused by the formation of AlN.

Discussion

From the analysis above, the schematic mechanism is shown in Fig. 14 for the protection and breakdown of oxide films on the HR3C (Fe–25Cr–20Ni) and the AFA austenitic stainless steel (Fe–22Cr–25Ni–2.5Al) oxidized at varying temperatures. As shown in Fig. 14a, the continuous and compact Cr_2O_3 scale can be formed on the surface of HR3C at temperatures of 700 or 800 °C, protecting the steel from high-temperature corrosion. When the oxidation temperature increases to a higher temperature (900 or 1000 °C), the diffusion of Mn element quickened from the matrix into the surface of Cr_2O_3, leading to the partial transformation of the Cr_2O_3 into loose spinel $MnCr_2O_4$ on the outermost layer. Moreover, the loose and porous structure makes some Cr_2O_3 volatilize at high temperature and internal Cr_2O_3 was formed under the $MnCr_2O_4$ scale; as a result, the oxidation of HR3C was exacerbated, as shown in Fig. 14b.

When the 22Cr–25Ni–2.5Al AFA steel was employed at the temperature of 700 or 800 °C, the formation of Al_2O_3 oxide layer has a priority over Cr_2O_3, because the Al/Al_2O_3 is more thermodynamically stable than Cr/Cr_2O_3 in air. The continuous and contacting Al_2O_3 oxide layer can significantly enhance the high-temperature oxidation resistance, which is shown in Fig. 14c. However, as shown in Fig. 14d, the spinel $MnCr_2O_4$ can also be formed on the surface of 22Cr–25Ni–2.5Al AFA steels oxidized at 900 or 1000 °C, and a large amount of fine Al_2O_3 and needle-like or block-like AlN was produced in the vicinity of the oxide layer. Owing to the internal oxidation and nitrogen for the 22Cr–25Ni–2.5Al AFA steels, they would

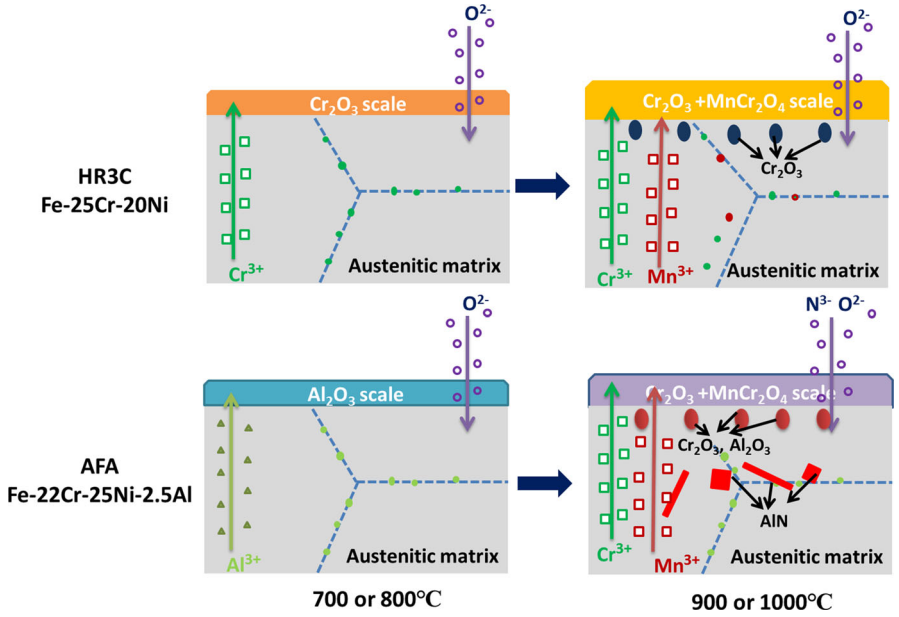

Fig. 14 Schematic mechanism for the protection and spallation of oxide films on the HR3C (Fe–25Cr–20Ni) and the AFA austenitic stainless steels (22Cr–25Ni–2.5Al) oxidized at different temperatures

have a worse oxidation resistance than HR3C at relatively high temperatures, which explains the oxidation kinetics of the two alloys shown in Fig. 1. The significant generation of internal Al_2O_3 and AlN would further deprive the Al elements of the alloys, not effectively providing the Al source of stable Al_2O_3 and eventually producing the Cr-rich and Mn-rich oxides. However, it is still worth exploring why the internal Al_2O_3 and AlN were initially formed instead of protective, continuous alumina when the temperature was increased.

Conclusions

The oxide film of HR3C and 22Cr–25Ni–2.5Al AFA alloys was investigated after oxidization at 700, 800, 900 and 1000 °C for 120 h. The entire oxidation kinetic curve was fitted to follow the parabolic law, and the 22Cr–25Ni–2.5Al AFA alloys exhibited better oxidation resistance than HR3C. When the alloys were oxidized at a relatively low service temperature (700 or 800 °C), the addition of aluminum elements changed the composition and structure of the oxide film, resulting in the transformation of the outer layer oxides from Cr_2O_3 to an Al-containing oxide. The Al_2O_3 film on the surface is more compact than the Cr_2O_3 film and improves the oxidation resistance of the alloys at high temperatures.

After oxidation at 900 or 1000 °C for 120 h, the oxide film starts peeling off and the oxide thickness on the alloy is significantly higher than that oxidized at 700 or 800 °C. The oxide film on HR3C and 22Cr–25Ni–2.5Al AFA alloys oxidized at 900 or 1000 °C shows an outer layer mainly composed of Cr_2O_3 and $MnCr_2O_4$, owing to the high diffusion rate of Mn at these temperatures. For HR3C, an internal Cr_2O_3 oxide was formed underneath this outer loose layer; however, for 22Cr–25Ni–2.5Al AFA steel, a certain amount of subscale internal alumina and internal aluminum nitride emerged near the oxide layer. The loose oxide film accelerates the diffusion of nitrogen, resulting in the formation of a large amount of internal AlN, making the oxidation resistance of 22Cr–25Ni–2.5Al AFA alloys worse than that of HR3C at the relatively high temperatures.

Acknowledgements This research was supported by the Natural Science Foundation of Shanxi Province (2014011002) and Natural Science Foundation for Young Scientists of Shanxi Province (201601D202033).

References

1. T. Hussain, A. U. Syed, and N. J. Simms, *Oxidation of Metals* **80**, 529 (2013).
2. R. Viswanathan, K. Coleman, and U. Rao, *International Journal of Pressure Vessels & Piping* **83**, 778 (2006).
3. F. Msuyama, *Isij International* **41**, 612 (2001).
4. Z. Yue, M. Fu, X. Wang, and X. Li, *Oxidation of Metals* **77**, 17 (2012).
5. J. Fu, N. Li, Q. Zhou, and P. Guo, *Oxidation of Metals* **83**, 317 (2015).
6. J. Zhao, H. Wang, C. Q. Cheng, Y. Y. Fang, and X. N. Li, *Materials at High Temperatures* **32**, 461 (2015).
7. Z. Zhang, Z. Hu, H. Tu, S. Schmauder, and G. Wu, *Materials Science & Engineering A* **681**, 74 (2017).

8. B. Wang, Z. D. Liu, S. C. Cheng, C. M. Liu, and J. Z. Wang, *Journal of Iron and Steel Research International* **21**, 733 (2014).
9. J. T. Yuan, W. Wang, H. H. Zhang, L. J. Zhu, S. L. Zhu, and F. H. Wang, *Corrosion Science* **109**, 36 (2016).
10. T. Dudziak, M. Łukaszewicz, N. Simms, and J. R. Nicholls, *Corrosion Engineering Science & Technology* **50**, 272 (2015).
11. S. Tang, S. Zhu, X. Tang, H. Pan, and Z. D. Xiang, *Corrosion Science* **82**, 255 (2014).
12. Y. Xu, X. Zhang, L. Fan, J. Li, X. Yu, X. Xiao, and L. Jiang, *Corrosion Science* **100**, 311 (2015).
13. T. Liu, C. Wang, H. Shen, W. Chou, N. Y. Iwata, and A. Kimura, *Corrosion Science* **76**, 310 (2013).
14. Y. Yamamoto, M. P. Brady, Z. P. Lu, P. J. Maziasz, C. T. Liu, B. A. Pint, K. L. More, H. M. Meyer, and E. A. Payzant, *Science* **316**, 433 (2007).
15. M. P. Brady, J. Magee, Y. Yamamoto, D. Helmick, and L. Wang, *Materials Science & Engineering A* **590**, 101 (2014).
16. N. M. Yanar, B. S. Lutz, L. Garcia-Fresnillo, M. P. Brady, and G. H. Meier, *Oxidation of Metals* **84**, 1 (2015).
17. X. Q. Xu, X. F. Zhang, G. L. Chen, and Z. P. Lu, *Materials Letter* **65**, 3285 (2011).
18. D. Q. Zhou, W. X. Zhao, H. H. Mao, Y. X. Hu, X. Q. Xu, X. Y. Sun, and Z. P. Lu, *Materials Science & Engineering A* **622**, 91 (2015).
19. Y. Qiao, J. Wang, Z. Zhang, X. Quan, J. Liu, X. Fang, and P. Han, *Oxidation of Metals* 2017. https://doi.org/10.1007/s11085-017-9738-0.
20. N. Dong, Y. Qiao, C. Zhang, J. Wang, G. Fan, X. Fang, and P. Han, *RSC Advances* **7**, 15727 (2017).
21. A. Col, V. Parry, and C. Pascal, *Corrosion Science* **114**, 17 (2017).
22. X. Peng, J. Yan, Y. Zhou, and F. Wang, *Acta Materialia* **53**, 5079 (2005).
23. A. M. Huntz, A. Reckmann, C. Haut, C. Sévérac, M. Herbst, F. C. T. Resende, and A. C. S. Sabioni, *Materials Science & Engineering A* **447**, 266 (2007).
24. N. R. Karimi and F. Riffard, *Applied Surface Science* **254**, 2292 (2008).
25. M. P. Brady, G. Muralidharan, Y. Yamamoto, and B. A. Pint, *Oxidation of Metals* **87**, 1 (2017).
26. M. P. Brady, K. A. Unocic, M. J. Lance, M. L. Santella, Y. Yamamoto, and L. R. Walker, *Oxidation of Metals* **75**, 337 (2011).
27. M. P. Brady, Y. Yamamoto, M. L. Santella, and L. R. Walker, *Oxidation of Metals* **72**, 311 (2011).
28. M. P. Brady, Y. Yamamoto, B. A. Pint, M. L. Santella, P. J. Maziasz, and L. R. Walker, *Materials Science Forum* **595**, 725 (2008).
29. R. Elger and R. Pettersson, *Oxidation of Metals* **82**, 469 (2014).
30. H. E. Evans, D. A. Hilton, R. A. Holm, and S. J. Webster, *Oxidation of Metals* **14**, 235 (1980).